Understanding and control of the metallic state in epitaxial NdNiO3

Guo, Qikai

DOI:
10.33612/diss.180302851

Chapter 4

Tunable resistivity exponents in the metallic phase of epitaxial nickelates

We report a detailed analysis of the electrical resistivity exponent of thin films of $NdNiO_3$ as a function of epitaxial strain. Thin films under low strain conditions show a linear dependence of the resistivity *versus* temperature. In addition, the apparent temperature exponent, n, can be tuned with the epitaxial strain between n= 1 and n= 3. We discuss the critical role played by quenched random disorder in the value of n. Our work shows that the assignment of Fermi/Non-Fermi liquid behaviour based on experimentally obtained resistivity exponents requires an in-depth analysis of the degree of disorder in the material.

4.1 Introduction

The tunable resistivity of materials undergoing a metal-insulator transitions (MIT) holds great promise for resistive switching applications, such as adaptable electronics and cognitive computing [1–7]. However, a complete understanding of the metallic phase in these strongly correlated electron systems is still one of the central open problems in condensed matter physics [8, 9].

Electronic transport is generally explained by means of Boltzmann's theory, which considers a fluid of free quasi-particles that scatter occasionally. In normal metals, the resistivity increases linearly with temperature as electrons are more strongly scattered by lattice vibrations. At low temperatures, interactions between electrons can significantly affect the electrical properties and give rise to a T^2 dependence of resistivity, according to Landau's Fermi liquid (FL) theory [10]. Therefore, the scaling exponent of the power law term of the resistivity as a function of temperature (n) is often used to infer the type of interactions ruling the metal state. In materials with strong electron-electron interactions and undergoing ordering phenomena, other exponents ($n \neq 1, 2$) are usually observed, being the physics behind this so-called "Non-Fermi liquid" (NFL) behaviour [11–13] a subject of active discussion [14–17].

Among strongly correlated electron materials, nickelates ($RENiO_3$, with RE de-

noting a trivalent rare earth element) present a very interesting case. They have attracted attention due to their MIT [18] and the possibility to tune it using different RE elements or by epitaxial strain [19–24]. Bad metallic behaviour in nickelates has also been claimed [25]. Different models for the origin of the MIT have been put forward, based on either positive or negative charge transfer as responsible for the insulating state [26–34]. The negative charge transfer model supports the bond disproportionation picture and is strongly supported by recent experiments [35–37]. Independent from the exact microscopic picture, the origin of the MIT is a cooperative lattice distortion that reduces the symmetry from a high-temperature orthorhombic phase to a low-temperature monoclinic phase, involving two Ni sites, with the associated need for cooperative accommodation of different Ni-O bond-lengths [38]. Remarkably, it has been reported that eliminating the MIT in nickelates by orbital engineering would give rise to a superconducting state [39], with a very recent experimental achievement in this direction [40]. It becomes, then, important to have an accurate picture of the relevant electron interactions in the intermediate and low temperature regimes, just before the MIT takes place. However, despite the vast amount of recent works, the metallic behaviour of the nickelates is not yet fully understood.

In nickelates, different n-exponents of the resistivity as a function of temperature have been reported [14, 25, 41–46]. Linear dependence with temperature has been measured in the whole $Nd_xLa_{1-x}NiO_3$ series in ceramic pellets[41]. Liu *et al*. [42] obtained n= 5/3 and n= 4/3 for $NdNiO_3$ (NNO) films under compressive strain, while Mikheev *et al*. reported a crossover between FL (n=2) and NFL (n=5/3) in NNO films with varying epitaxial strain [43]. The need of an empirical parallel resistor model to introduce the effect of the saturation resistivity rises questions about the interpretation of the *apparent* (experimentally obtained) exponents, as discussed by Hussey *et al.* [47].

Here, we report the evolution of the resistivity exponent of $NdNiO_3$ under different degrees of epitaxial strain. Strain-free (bulk like) thin films show a linear temperature dependence of the resistivity (n=1). The combined effect of epitaxial strain and random disorder produces a continuous departure from n=1, in agreement with recent theoretical work by Patel *et al*. [48].

4.2 Experimental methods

Epitaxial $NdNiO_3$ thin films were deposited on single-crystal $LaAlO_3$ (LAO), $NdGaO_3$ (NGO), $SrTiO_3$ (STO) and $DyScO_3$ (DSO) substrates by pulsed laser ablation of a single-phase target (Toshima Manufacturing Co., Ltd.). The quality of the target is of crucial importance to attain reproducibility of the film properties, as reported in [49]. Before deposition, the LAO substrates were thermally annealed at 1050 °C in a

flow of O_2 and etched with DI water to obtain an atomically flat surface with single terminated terraces. The NGO and STO substrates were etched with buffered NH_4F (10 M)-HF solution (BHF) and the DSO substrates were etched with NaOH. All the substrates displayed single terminated terraces after the treatment. The substrates were heated to a temperature of 700 °C prior to the deposition of the films and were kept at that temperature during growth. Oxygen was present in the growth chamber during deposition with an oxygen pressure of 0.2 mbar and the laser fluence on the target was 2 J/cm^2. After deposition, the samples were cooled down to room temperature at 5 °C/min with a oxygen pressure of 900 mbar. The growth was monitored using Reflection High Energy Electron Diffraction (RHEED). The films showed a constant deposition time of about 22 seconds per unit cell (s/uc) for NNO/LAO and 24 s/uc for NNO/STO. Films with various thicknesses were grown by precisely tuning the deposition time. The oxygen deficient NNO films were grown on STO and LAO substrates followed by a vacuum annealing process at 10^{-7} mbar. The concentration of oxygen vacancies in these films is tuned by annealing the specimens in tube furnace with a oxygen-enriched environment (400 cc/min and atmospheric pressure) and step-by-step increased temperature. The annealing time for each step is one hour.

The thicknesses, crystal orientation and phase purity of the films, as well as the epitaxial relation between film and substrates, were assessed using X-ray diffraction by means of 2θ-ω scans and reciprocal space maps (RSM), respectively, on a Panalytical, Xpert MRD Pro diffractometer. Cross-sectional specimens of the films were prepared and studied by scanning transmission electron microscopy (STEM) on a probe corrected FEI Titan 60–300 microscope equipped with a high-brightness field emission gun (X-FEG) and a CEOS aberration corrector for the condenser system. This microscope was operated at 300 kV. High angle annular dark field (HAADF) STEM images were acquired with a convergence angle of 25 mrad and a probe size below 1 Å. The strain state of the films was determined by geometrical phase analysis (GPA) of these HAADF images.

Electrical transport properties were measured between 5 K to 400 K by the van der Pauw method in a Quantum Design Physical Property Measurement System (PPMS), using a Keithley 237 current source and a Agilent 3458A multimeter.

4.3 Results

4.3.1 Tuning the resistivity-temperature exponent.

Crystalline NNO films have been grown by pulsed laser deposition (PLD) on <001> oriented LAO, NGO, STO substrates and <110> oriented DSO substrates, using a single-phase ceramic target (see the Methods for more details). Perovskite NNO possesses an orthorhombic structure with a pseudo-cubic lattice parameter of 3.807 Å, which is slightly larger than that of the LAO substrate (3.790 Å). Thus, the films on LAO are expected to be subjected to small compressive strain. On the contrary, the films grown on NGO (3.858 Å), STO (3.905 Å) and DSO (3.955 Å) substrates should experience increasing tensile strain. Fig. 4.1(a) shows the typical atomic force microscope (AFM) topography image of a 5 nm NNO film grown on a LAO substrate (NNO/LAO), showing that the atom-high steps from the substrate are still visible after the deposition of the film. *In-situ* high energy electron diffraction (RHEED) intensity oscillations recorded during the film growth indicate that at least the first 13 layers ($\sim$ 5 nm) of NNO film are deposited atomic-layer by atomic-layer (see Fig. 4.1(b)).

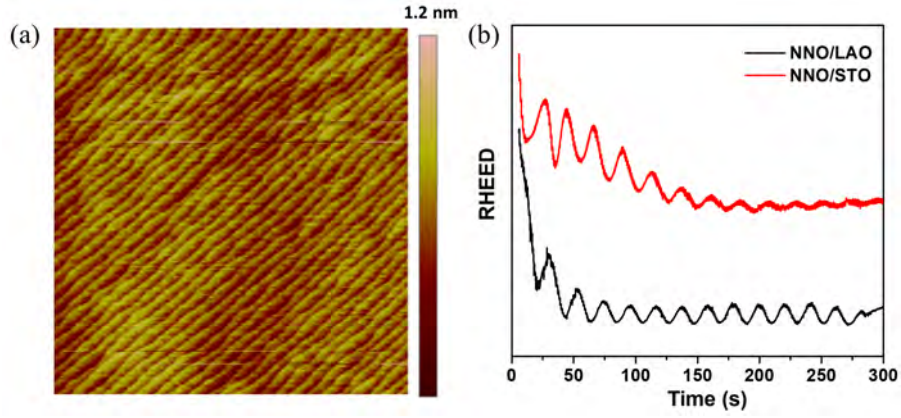

Figure 4.1: *Growth of nickelate films. (a) RHEED intensity oscillations observed in-situ during PLD deposition. (b) AFM topography image of a 5×5 μm× μm area in a 5 nm thick NNO film grown on a LAO substrate.*

Fig. 4.2(a) and (b) shows the sheet resistance ($R_{\square}$) of NNO films grown on LAO and STO substrates, respectively, as a function of temperature. The NNO films grown on LAO substrates (under small compressive strain) exhibit a sharp MIT and a pronounced thermal hysteresis; while the hysteresis is strongly reduced in the NNO/STO films, in agreement with previous reports [1]. The evolution of the

first order transition towards a continuous, percolative-like metal-insulator transition is consistent with the presence of quenched random disorder in the films grown on STO [50]. This interpretation is supported by a higher resistivity and a smaller residual resistivity ratio in these films compared to those grown on LAO. A further distinction is observed in the evolution of the metal-insulator transition temperature (T_{MI}) as a function of thickness (see insets to Fig. 4.2(a) and (b)), which has been attributed to the opposite alteration of orbital polarization in response to different sign of the epitaxial strain [51].

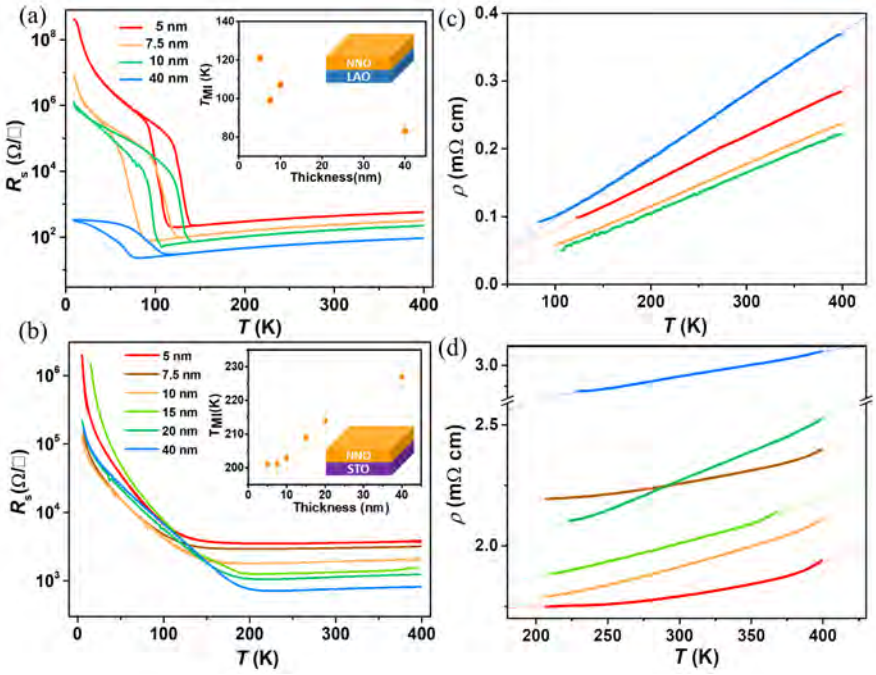

Figure 4.2: *Temperature-dependent resistivity. Temperature dependence of the sheet resistance($R_{\square}$) both during cooling and heating for NNO thin films grown on (a) LAO and (b) STO substrates with different thickness. Inset shows the metal-insulator transition temperature (T_{MI}) as a function of thickness. The T_{MI} is extracted from the resistivity data during the cooling down process. The resistivity as a function of temperature in the metallic phase of NNO thin films grown on (c) LAO and (d) STO substrates with different thickness. The thin solid lines are fits using Eq. (4.1).*

Like in most of metals, the electrical resistivity in the metallic state of nickelates can be fitted using a power law:

$$\rho(T) = \rho(0) + AT^n \tag{4.1}$$

where A is a coefficient related to the strength of electron scattering and n is the apparent power law exponent. As shown in Fig. 4.2(c), the metallic resistivity of all NNO films grown on LAO substrates in the measured temperature range (from T_{MI} to 400 K) can be well described with a linear temperature dependence (n=1.00$\pm$ 0.01), independent of film thickness. This temperature dependence has been observed in other systems, ranging from cuprates to heavy fermions, in spite of their different mechanisms of electron scattering [52]. What they have in common, however, is a constant scattering rate per kelvin ($\approx k_B/\hbar$), indicating that the excitations responsible for scattering are governed only by temperature. On the other hand, in the case of NNO/STO films (Fig. 4.2(d)), the temperature-resistivity scaling of films with different thickness deviates from linearity, showing the departure from this intrinsic mechanism.

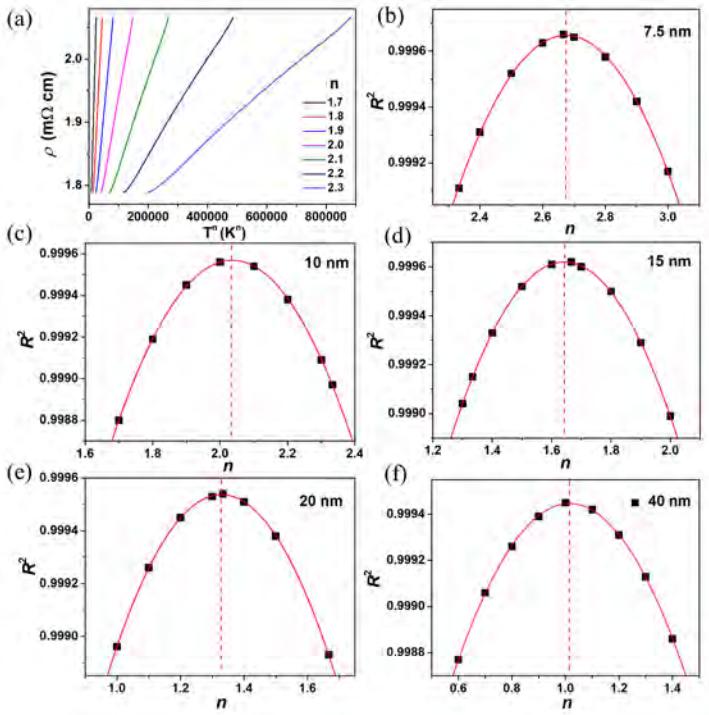

Figure 4.3: *Extraction of exponents (n). Resistivity of a 10 nm NNO/STO film as a function of T^n with different n values. (b-f) The coefficient of determination (R^2) as a function of n for NNO/STO films with thicknesses of 7.5 nm, 10 nm, 15 nm, 20 nm and 40 nm, respectively.*

It is important to pay attention to the extraction of the ρ(T) power law exponents from the experimental data. Proper determination of scaling exponents requires ac-

cess to many scales in the experimental parameters. In the case of temperature scaling, this is not possible so the exponents obtained from the experimental resistivity-temperature analysis can be considered as *apparent* scaling exponents. In order to extract these exponents, the experimentally obtained ρ(T) of each film was plotted as a function of T^{n} for different n values, as shown for one of the films in Fig. 4.3(a). All the different curves were fitted as linear fits and the best fit (the best n) was determined by the largest R^2 factor. This was done by interpolating to the maximum of the R^2 parabola, as shown for several examples in Fig. 4.3(b-f). The range of validity of the fits was checked by plotting the temperature derivative of ρ(T) as a function T^{n}. These plots can be seen for some of the films in Fig. 4.4.

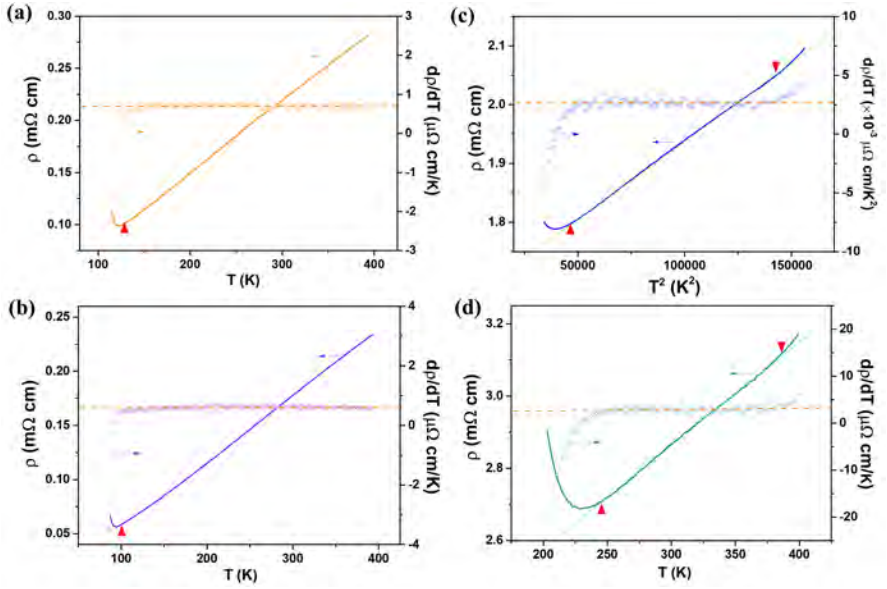

Figure 4.4: *Resistivity (solid lines) and its temperature derivative (open circles) versus T^n for NNO/LAO films with thickness of 5 nm (a) and 7.5 nm (b) and for NNO/STO films with thicknesses of 10 nm (c) and 40 nm (d). The upturn in resistivity signalling the metal-insulator transition is visible. The red triangles signal the temperature region where the resistivity starts to deviate from the best fit.*

The values of n and A-coefficients in both NNO/LAO and NNO/STO systems are shown, as a function of thickness, in Fig. 4.5(a). Interestingly, n shows a clear evolution with thickness in the NNO/STO films: n decreases with increasing NNO/STO film thickness from a value of n= 3.00± 0.05 for a 5 nm film to an apparent linear dependence (n= 1.01± 0.01) for the thickest film (40 nm). To understand this behaviour we turn to an in-depth structural characterization of the films.

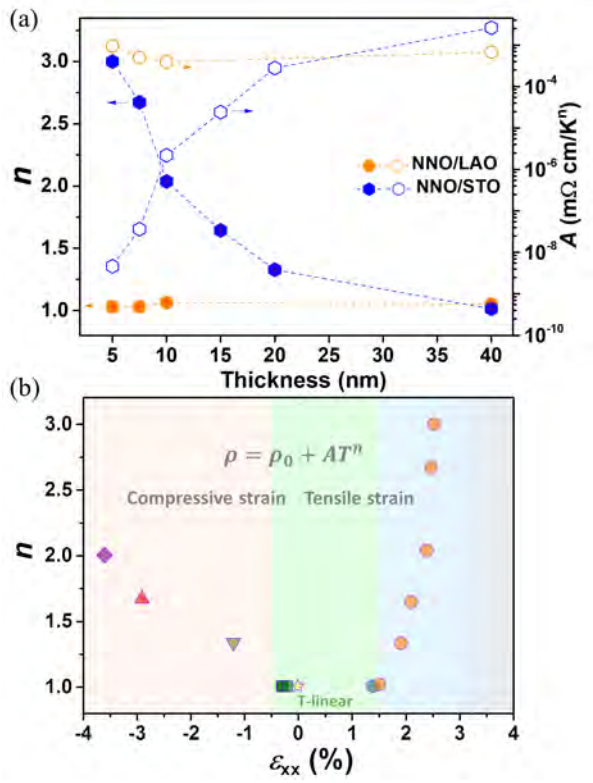

Figure 4.5: *Tunable exponents. (a) Power law exponents (n) and A-coefficients from Eq. (1), extracted from the fits in Fig. 1 (c,d) as a function of film thickness. The error bars are determined as described in Supplementary Note 2. (b) Scaling exponent (n) as a function of in-plane strain (ε_{xx}). The data are for films grown on different substrates: LAO (squares), NGO (hexagon) and STO (circles). The highly tensile region shadowed in grey denotes the insulating state observed for the films on DSO. In addition, we also plot n of bulk NNO [41] (star), as well as that for epitaxial NNO films under compressive strain reported by Liu et al. [42] (triangles) and Mikheev et al. [43] (rhombus).*

Fig. 4.6(a) and (b) show the diffraction patterns for films grown on LAO and STO, respectively. The presence of Laue fringes indicates the high quality of the interfaces. The different sign of the epitaxial strain on the two substrates can be assessed by the different relative positions of the film and substrate peaks. Reciprocal space maps (RSM) around the $(103)_{pc}$ peaks, are shown in Fig. 4.6(c-h). All NNO films grown on LAO grow coherently with the substrate (with coincident in-plane reciprocal lattices of film and substrate), for all investigated thicknesses, as expected from the very similar lattice of the bulk NNO (signalled in the maps by the yellow

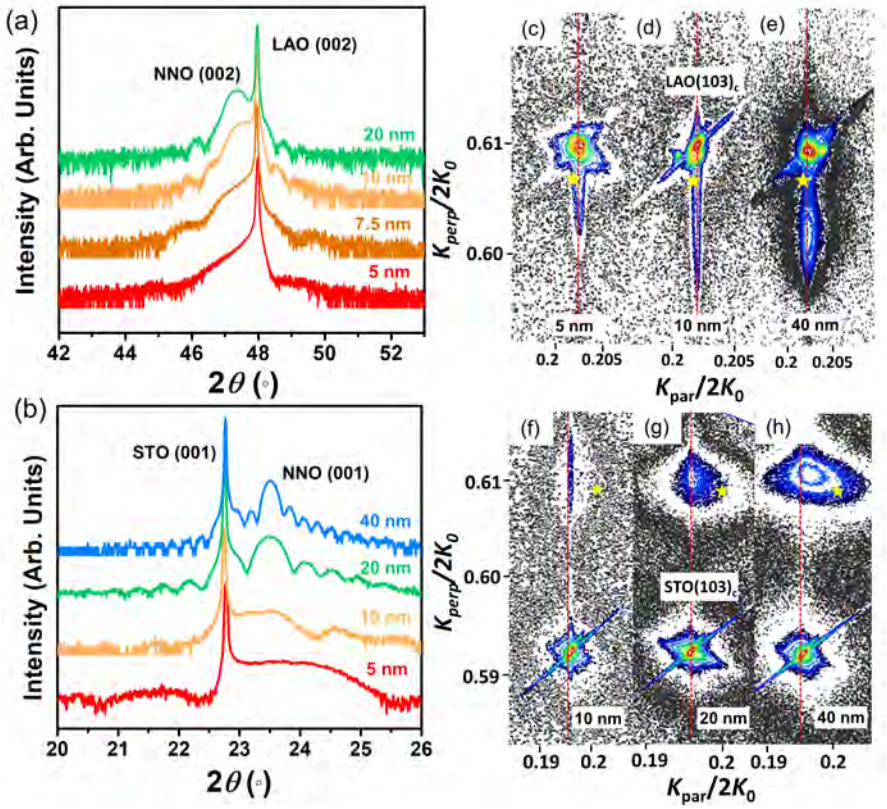

Figure 4.6: *Structural characterization. X-ray diffraction patterns around the 002-reflection of NNO/LAO films (a) and around the 001-reflection of NNO/STO films (b) with different thicknesses. Reciprocal space map (RSM) around the $(103)_c$ diffraction peaks of (c) 5 nm, (d) 10 nm, (e) 40 nm NNO/LAO films and (f) 10 nm, (g) 20 nm, (**h**) 40 nm NNO/STO films. The abscissa, K_{perp}, (ordinate, K_{par},) represents the in-plane (out-of-plane) component of the scattering vector. Both are normalized by $2k_0 = 4\pi/\lambda$. The red dashed lines are guides to the eyes showing the substrate in-plane lattice. The yellow stars signals the $(103)_c$ peak of bulk NNO.*

stars) and the substrate. On the contrary, in the NNO/STO films, only the thinnest films grow coherently with the substrate and show an in-plane lattice significantly larger than that of the bulk, due to the large differences between the bulk NNO and the STO substrate lattices. For increasing thicknesses, a gradual shift of the film peak can be observed, in agreement with the expected evolution of the lattice parameters and strain relaxation toward the bulk lattice, with increasing thickness. Thus, the observed evolution of n (Fig. 4.5(a)) corresponds to the gradually relaxed in-plane

Table 4.1: *The in plane strain (ε_{xx}) of NNO films with different thickness grown on different substrates.*

	5 nm	7.5 nm	10 nm	15 nm	20 nm	40 nm
NNO/LAO	-0.3 %	-0.29 %	-0.27 %	×	×	-0.20 %
NNO/NGO	+1.34 %	×	×	×	×	×
NNO/STO	+2.54 %	+2.48 %	+2.40 %	+2.11 %	+1.92 %	+1.52%
NNO/DSO	×	×	+3.86 %	×	×	×

strain of the films.

Fig. 4.5(b) summarizes the n values extracted from the NNO films as a function of the in-plane strain, ε_{xx}, obtained from the diffraction data in Fig. 4.6. To calculate the in-plane strain (ε_{xx}), the in-plane lattice parameter (a) of each film is obtained by performing a reciprocal space map scanning around the $(103)_{pc}$ peak. For this, the value of $k/2k_0$ at the center of the film peak is extracted and then the in-plane lattice parameter is calculated according to:

$$\frac{k}{2k_0} = \frac{\frac{2\pi}{a}}{2\frac{2\pi}{\lambda}} \tag{4.2}$$

where λ is the wavelength of the X-ray (1.5406 Å in our case). The in-plane strain of the film is then calculated with respect to the unit cell volume of bulk $NdNiO_3$ as:

$$\varepsilon_{xx} = \frac{a - a_b}{a_b} \tag{4.3}$$

where $a_b = V^{1/3}$, being V the unit cell volume of bulk $NdNiO_3$. The ε_{xx} of all films is presented in Table 1.

Data from NNO films on NGO substrates (ε_{xx}= +1.34 %) are also included. A 5 nm NNO/NGO film also shows apparent linear T scaling in the metallic phase, confirming the correlation between the magnitude of the tensile strain and n (see Fig. 4.7). Similarly to the films on STO, the extended resistivity data of the NNO/NGO films (inset of Fig. 4.7) also shows a reduced hysteresis compared to that of the films on LAO. Fig. 4.5(b) is completed with n values reported by other authors for bulk NNO [41] and NNO films under larger compressive strains [42, 43]. Indeed, we observe a clear dependence of n on the in-plane strain. Both tensile and compressive strains are expected to induce an increase of the orbital splitting between the Ni^{3+} $x^2 - y^2$ and $3z^2 - r^2$ e_g levels [43]. However, the large asymmetry observed, with a significantly stronger dependence for the tensile strain regime, points to an additional influence on n.

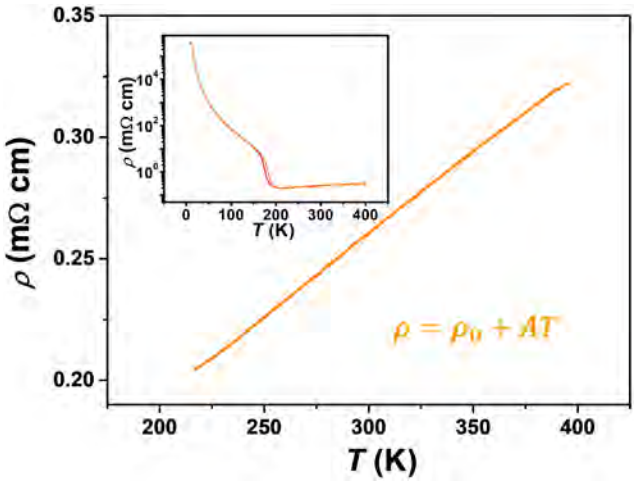

Figure 4.7: *Temperature-dependent resistivity of NNO films on NGO. T-linear dependent resistivity in the metallic phase of a 5 nm NNO/NGO film. Inset: Temperature dependence of resistivity in an extended temperature range, including both cooling and heating processes.*

4.3.2 Interplay between strain and defect formation.

In order to shed light into this behaviour, we performed scanning transmission electron microscopy (STEM) on the films. Cross-sectional specimens of the films were studied by atomic resolution STEM (for experimental details, see Methods). The high-angle annular dark-field (HAADF) STEM image shown in Fig. 4.8(a) evidences the epitaxial, cube-on-cube growth of a 5 nm thick NNO film on a LAO substrate, with a flat, atomically sharp interface. No defects or misfit dislocations are observed. The strain state of the films was determined by geometrical phase analysis (GPA) of the HAADF images, the deformation of the in-plane lattice parameter of the film respect to the substrate (ε_{xx}) is depicted in Fig. 4.8(b). ε_{xx} is virtually zero across the 5 nm NNO film, showing a good in-plane lattice match between film and substrate, in agreement with the x-ray diffraction data. A thicker NNO film on LAO substrate also shows ε_{xx}= 0 across most of the film but it starts showing small regions with Ruddlesden-Popper (RP) faults, often reported in nickelates [53], as seen in Fig. 4.8(c-d). Some effect of these RP defects can be seen in the electrical properties, which show a strongly decreased resistance in the insulating state (Fig. 4.2(a)), as well as a increased resistivity in the metallic state for the 40 nm films on LAO (Fig. 4.2(c)). However, the RP defects do not preclude the presence of hysteresis at the metal-insulator transition, nor the apparent linear behaviour of the metallic resistivity in Fig. 4.2(c), as it will be discussed in detail later. RP faults are known to have a significantly enlarged out-of-plane lattice parameter [53], which can explain the

unusual evolution of the out-of-plane lattice parameters as a function of thickness for the NNO/LAO films, shown in Fig. 4.6(a). Similar images for the thinnest and the thickest films on STO, shown in Fig. 4.9, reveal a higher abundance of RP faults, which are present even in the thinnest films. The data, thus, strongly suggest that the RP secondary phases present in the films, are not correlated with the observed changes of n.

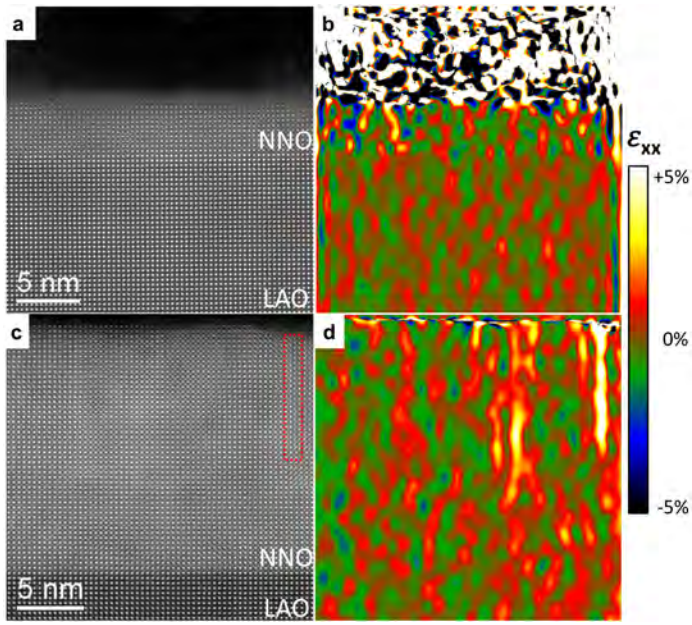

Figure 4.8: *Atomic image and strain in NNO/LAO. Cross-sectional HAADF-STEM image of $NdNiO_3$ thin films grown on a $LaAlO_3$ substrates, for a 5 nm thick film (a) and a 20 nm thick film (b). The respective in-plane components of the strain tensor (ε_{xx}, colour scales) obtained from the STEM images by geometrical phase analysis (GPA) are shown in (b) and (d). The red dashed lines surround the RP faults.*

The effect of strain on n may be indirect. Planar defects such as misfit dislocations or stacking faults have been often observed in nickelate films [54] and the creation of oxygen vacancies is known to be an efficient mechanism to relax tensile strain in epitaxially grown perovskites, as oxygen vacancies locally enlarge the lattice [22, 24, 55–58]. In nickelate thin films, a pair of oxygen vacancies favour the reduction of the Ni ions to Ni^{2+} [6, 59, 60]. Indeed, measurement of Seebeck coefficients on films with a thickness of 10 nm grown on LAO and STO, plotted in Fig. 4.10(a), show that while the film on LAO displays metallic-like transport, the film on STO shows a flat temperature dependence, characteristics of polaronic systems.

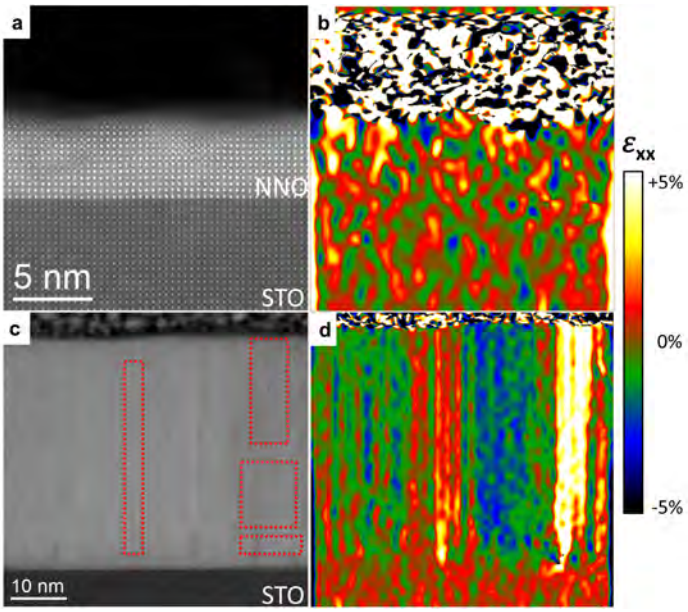

Figure 4.9: *Atomic image and strain in NNO/STO. Cross-sectional HAADF-STEM image of $NdNiO_3$ thin films grown on a $SrTiO_3$ substrates, for a 5 nm thick film (a) and a 40 nm thick film (c). The respective in-plane components of the strain tensor (ε_{xx}, colour scales) obtained from the STEM images by geometrical phase analysis (GPA) are shown in (b) and (d). The red dashed lines surround the RP faults.*

Another indication of the existence of an increased content of oxygen vacancies in our films on STO comes from the structural data. From the definition of Poisson ratio, ν, the pseudo-cubic lattice parameters that would correspond to the unstrained case for the different films can be estimated as $a_o = (2\nu a+(1-\nu)c)/(1+\nu)$ [61, 62], where a and c are the in-plane and out-of-plane lattice parameters of the films, respectively, obtained from the structural data of Fig. 4.6, and ν= 0.30 has been used for all films. The results, plotted in Fig. 4.10(b), show that the films on LAO display a lattice volume close to the bulk value, while the unit cell volume of the films on STO is significantly increased, which is consistent with a larger oxygen vacancy content that decreases with increasing thickness. Moreover, the residual resistivity ratio (RRR), which is often used as a measurement of materials purity, increases with increasing thickness in the films on STO (Fig. 4.10(c)), also in agreement with a lower vacancy content in the thicker films.

Our experiments, therefore, indicate that NNO films subjected to relatively small strain values, display T-linear resistivity scaling. For larger values of tensile strain, an increase of the power law resistivity-temperature exponent with the magnitude

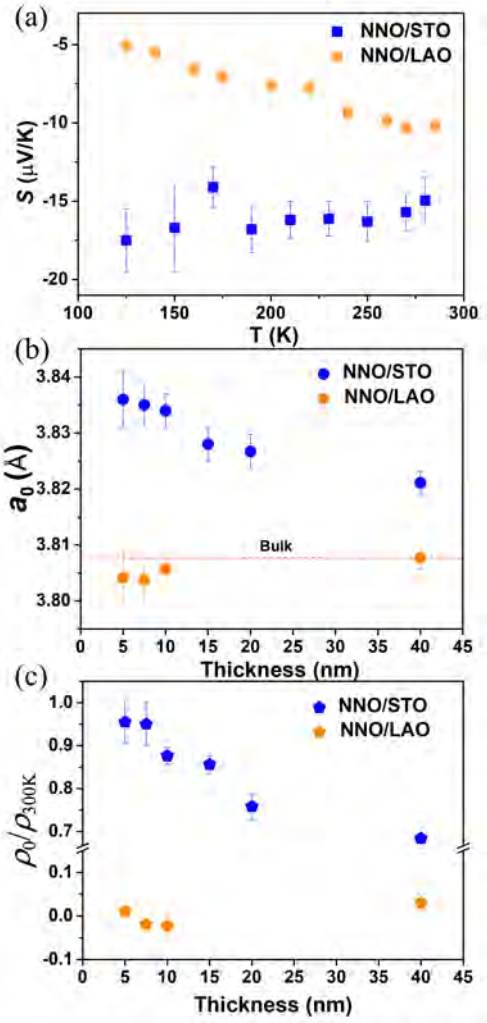

Figure 4.10: *Oxygen vacancy indicators. (a) Seebeck coefficients (S) measured on NNO films with thickness of 10 nm grown on LAO and STO substrates. (b) The unstrained film lattice parameter (a_0) and (c) the reversed residual-resistivity ratio (ρ_0/ρ_{300K}) of NNO films grown on LAO and STO substrates with different thickness. The error bar was determined from the deviation of repeated measurements.*

of the strain is observed. This is related to both the effect of strain on the orbital splitting and the degree of disorder, most likely due to oxygen vacancies, whose concentration is believed to increase with increasing tensile strain. These results

validate recent theoretical predictions by Patel *et al.* [48]. Their computational work uses the Anderson-Hubbard Hamiltonian to predict that the metallic state that arises for small and intermediate values of both the on-site Coulomb interaction of $3d$-electrons (U) and the disorder (V) can be continuously tuned. The calculations predict values varying from n= 1 to n= 2 by the joint action of both U and V (it is to be noticed that in our experiments larger values up to n= 3 are also observed). Interestingly, power law exponents varying with the degree of disorder have also been reported for $SrRuO_3$ thin films by Herranz *et al.* [63].

4.4 Discussion

In nickelates, epitaxial strain lifts the orbital degeneracy and causes orbital polarization of the e_g band: compressive strain lowers the energy of $3z^2 - r^2$ orbitals, while tensile strain lowers the $x^2 - y^2$ orbitals [43]. In this sense, both compressive and tensile strain have a similar influence on U. Since the amount of defects is smaller in the films under compressive strain, the values of n under epitaxial compression should be a closer measure of the direct effect of strain in the absence of disorder. On the other hand, the introduction of oxygen vacancies in the tensile case gives rise to a combined effect of strain and disorder, which is reflected in a stronger dependence with strain in tensile region of Fig. 4.5(b). Actually, to directly clarify the effect of disorder on n, a plot of n vs. defect density, instead of epitaxial strain as in Fig. 4.5(b) would be more appropriate.

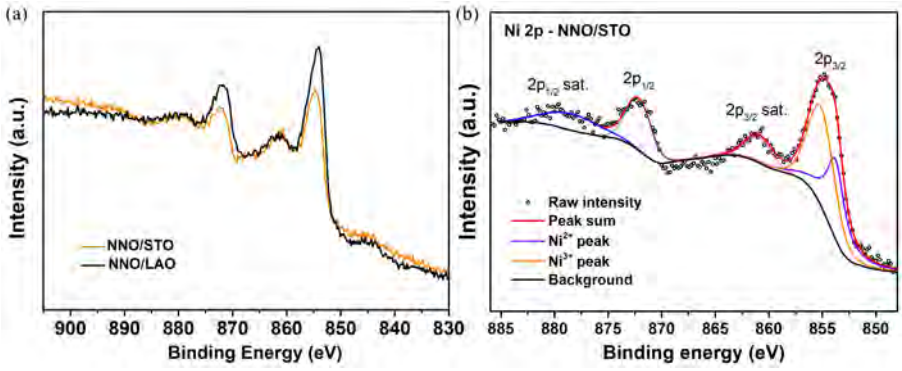

Figure 4.11: *XPS spectroscopy. (a) XPS spectra around the Ni 2p absorption edge of two 5 nm thick $NdNiO_3$ films grown on $SrTiO_3$ (orange line) and on $LaAlO_3$ (black line) substrates. (b) Spectra of the 5 nm thick $NdNiO_3$ film grown on $SrTiO_3$ showing the components of the fit.*

XPS characterization was conducted on a VG Microtech CLAM2 XPS system with a non monochromatic Al Kα source. All the measured spectra were fitted with a

Shirley-type background, including a shift due to charging, using the Au $4f_{7/2}$ XPS peak position as reference (see Fig. 4.11). The Ni $2p_{3/2}$ peak position obtained from the fit is 854.86 eV for the 5 nm thick NNO/STO film. This energy is in between those expected for the Ni^{3+} peak (855.9 eV) and the Ni^{2+} peak (853.9 eV), indicating the coexistence of both oxidation states. However, due to the experimental accuracy of the measurements ($\pm$ 0.8 eV), the extraction of an exact Ni^{3+}/Ni^{2+} ratio is impossible for us. In addition, the films on LAO also show coexistence of Ni^{2+} and Ni^{3+} peaks. This has also been reported by Preziosi *et al.*[49], which showed that even the samples with the sharpest MIT and resistance changes of nearly 6 orders of magnitude still showed a Ni^{2+}/Ni^{3+} ratio of about 0.2. This makes the quantification of the relative Ni^{2+} in the different samples very challenging. Hence, given the relationship between strain and defect concentration demonstrated by several authors [59, 64, 65], such a conservative plot is more adequate.

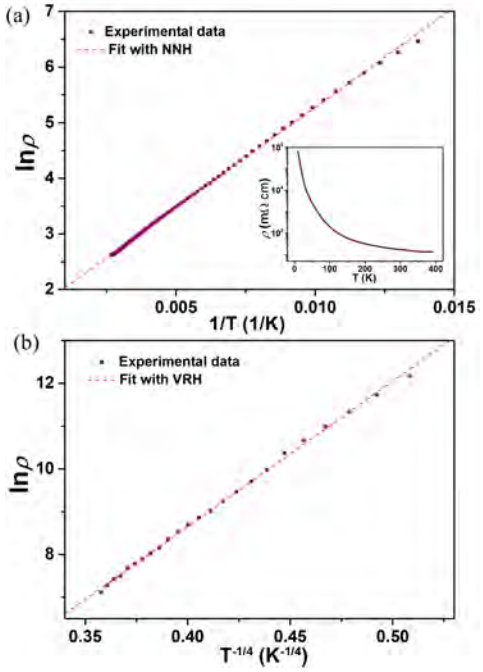

Figure 4.12: *Fit to resistivity of NNO/DSO. (a) $ln\rho$ versus T^{-1} for a 10 nm NNO/DSO film, together with the fit to a Near Neighbours Hopping (NNH) model (thermally-activated behaviour) with E_a=32 meV. A good agreement is found in a large temperature range down to about 70-80 K. Inset: Temperature dependence of resistivity in an extended temperature range. (b) $ln\rho$ versus $T^{-1/4}$ for the temperature range below 70 K, showing the fit to a 3D Variable Range Hopping (VRH) model.*

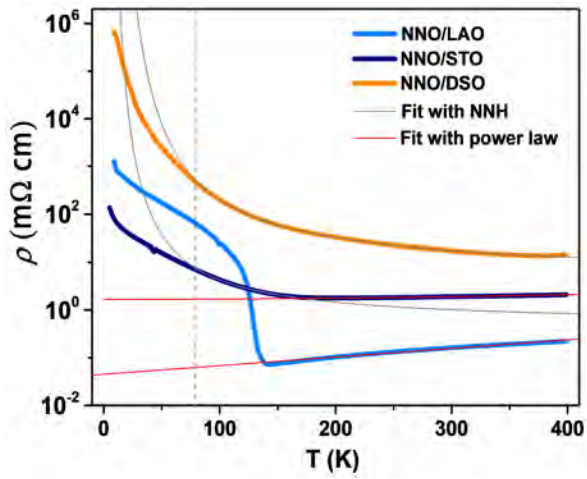

Figure 4.13: *Fit to resistivity with various models. ρ(T) curves of 10 nm NNO films grown on LAO, STO, and DSO substrates. The vertical dashed line indicates the temperature of crossover from the Variable Range Hopping (VRH) (fit not shown) to the Near Neighbours Hopping (NNH) regimes. The solid grey lines are the best fits in the NNH regime with activation energies of E_a= 32 meV and E_a= 20 meV, for the samples on DSO and on STO, respectively. The red solid lines are the best fits with power law in the metallic regime of the NNO films grown on LAO and STO substrates.*

Large enough tensile strain can induce a large density of oxygen vacancies and should, eventually, suppress the metallic phase. This is confirmed in films grown on DSO substrates, under +3.86 % strain, for which the resistivity data can be described by a variable range hopping (VRH) conduction model for $T < 70$ K (see Fig. 4.12) followed by a nearest neighbour hopping (NNH) model with E_a= 32 meV for temperatures above T= 70 K, as often observed in disordered solids [66, 67]. It is interesting to notice that a film of the same thickness on STO shows similar behaviour in the insulating state: comparable E_a in the NNH regime and comparable crossover temperature from VRH to NNH conduction (see Fig. 4.13). It is known that the presence of quenched disorder strongly impacts the transport properties inducing percolation and changing the nature of the phase transition [50]. In such percolation picture, a coexistence of metallic and insulating clusters could persist into the metallic phase. Indeed, the data of the films under intermediate strain (on STO) shows a magnitude of the resistivity in the metallic state that is in between those of the film on DSO and the film on LAO. It is worth to point out that oxygen vacancies can also order in nickelates, as recently shown both in thin films [54] and bulk crystals [68] of metallic $LaNiO_{3-\delta}$. The controlled tunability of oxygen vacancies with strain and its direct

relationship with the transport properties demonstrated could also be of importance in the context of the bond disproportionation and negative charge transfer models [35], as well as the recent work proposing the metal state as a bi-polaron liquid and the insulating phase as its ordered (bond-disproportionated) version [37].

4.5 Conclusion

To summarize, this work reports a clear evolution of the apparent scaling exponent of the resistivity-temperature characteristics (n) with strain and disorder, supporting recent theoretical predictions that show the tunability of the scaling exponents arising from the interplay between electron interactions and disorder in nickelates [48]. The overall picture helps to clarify that the underlying physics behind the observed evolution of exponents from T-linear to quadratic scaling and beyond, does not necessarily imply a crossover between FL and NFL behaviour or other exotic physics.

Bibliography

[1] R. Scherwitzl, P. Zubko, I. G. Lezama, S. Ono, A. F. Morpurgo, G. Catalan, and J.-M. Triscone, "Electric-field control of the metal-insulator transition in ultrathin $NdNiO_3$ films," *Adv. Mater.* **22**(48), pp. 5517–5520, 2010.

[2] T. Driscoll, H.-T. Kim, B.-G. Chae, M. Di Ventra, and D. Basov, "Phase-transition driven memristive system," *Appl. Phys. Lett.* **95**(4), p. 043503, 2009.

[3] A. McLeod, E. Van Heumen, J. Ramirez, S. Wang, T. Saerbeck, S. Guenon, M. Goldflam, L. Anderegg, P. Kelly, A. Mueller, *et al.*, "Nanotextured phase coexistence in the correlated insulator V_2O_3," *Nat. Phys.* **13**(1), p. 80, 2017.

[4] S. D. Ha, G. H. Aydogdu, and S. Ramanathan, "Metal-insulator transition and electrically driven memristive characteristics of $SmNiO_3$ thin films," *Appl. Phys. Lett.* **98**(1), p. 012105, 2011.

[5] S. D. Ha, J. Shi, Y. Meroz, L. Mahadevan, and S. Ramanathan, "Neuromimetic circuits with synaptic devices based on strongly correlated electron systems," *Phys. Rev. Appl.* **2**(6), p. 064003, 2014.

[6] J. Shi, S. D. Ha, Y. Zhou, F. Schoofs, and S. Ramanathan, "A correlated nickelate synaptic transistor," *Nat. Commun.* **4**, p. 2676, 2013.

[7] L. Wang, Q. Zhang, L. Chang, L. You, X. He, K. Jin, L. Gu, H. Guo, C. Ge, Y. Feng, *et al.*, "Electrochemically driven giant resistive switching in perovskite nickelates heterostructures," *Adv. Electron. Mater.* **3**(10), p. 1700321, 2017.

[8] V. Emery and S. Kivelson, "Superconductivity in bad metals," *Phys. Rev. Lett.* **74**(16), p. 3253, 1995.

[9] J. Zaanen, "Planckian dissipation, minimal viscosity and the transport in cuprate strange metals," *SciPost Phys.* **6**, p. 61, 2019.

[10] L. Landau, A. Abrikosov, and I. Khalatnikov, "The multiplicative renormalization group in the quantum theory of fields," *Sov. Phys. JETP* **3**(1), 1956.

[11] G. Stewart, "Non-Fermi-liquid behavior in d-and f-electron metals," *Rev. Mod. Phys.* **73**(4), p. 797, 2001.

[12] A. J. Schofield, "Non-Fermi liquids," *Contemp. Phys.* **40**(2), pp. 95–115, 1999.

[13] F. Rivadulla, J. Fernández-Rossier, M. García-Hernández, M. López-Quintela, J. Rivas, and J. Goodenough, "VO: A strongly correlated metal close to a Mott-Hubbard transition," *Phys. Rev. B* **76**(20), p. 205110, 2007.

[14] S. Stemmer and S. J. Allen, "Non-Fermi liquids in oxide heterostructures," *Rep. Prog. Phys.* **81**(6), p. 062502, 2018.

[15] A. Keller, L. Peeters, C. Moca, I. Weymann, D. Mahalu, V. Umansky, G. Zaránd, and D. Goldhaber-Gordon, "Universal Fermi liquid crossover and quantum criticality in a mesoscopic system," *Nature* **526**(7572), p. 237, 2015.

[16] S. Kasahara, T. Shibauchi, K. Hashimoto, K. Ikada, S. Tonegawa, R. Okazaki, H. Shishido, H. Ikeda, H. Takeya, K. Hirata, *et al.*, "Evolution from non-Fermi-to Fermi-liquid transport via isovalent doping in $BaFe_2(As_{1-x}P_x)_2$ superconductors," *Phys. Rev. B* **81**(18), p. 184519, 2010.

[17] S.-S. Lee, "Recent developments in non-Fermi liquid theory," *Annu. Rev. Condens. Matter Phys.* **9**, pp. 227–244, 2018.

[18] M. Imada, A. Fujimori, and Y. Tokura, "Metal-insulator transitions," *Rev. Mod. Phys.* **70**(4), p. 1039, 1998.

[19] M. L. Medarde, "Structural, magnetic and electronic properties of perovskites (R= rare earth)," *J. Phys. Condens. Matter* **9**(8), p. 1679, 1997.

[20] G. Catalan, R. Bowman, and J. Gregg, "Transport properties of $NdNiO_3$ thin films made by pulsed-laser deposition," *J. Appl. Phys.* **87**(1), pp. 606–608, 2000.

[21] G. Catalan, R. Bowman, and J. Gregg, "Metal-insulator transitions in $NdNiO_3$ thin films," *Phys. Rev. B* **62**(12), p. 7892, 2000.

[22] G. Catalan, "Progress in perovskite nickelate research," *Phase Transit.* **81**(7-8), pp. 729–749, 2008.

[23] S. Middey, J. Chakhalian, P. Mahadevan, J. Freeland, A. J. Millis, and D. Sarma, "Physics of ultrathin films and heterostructures of rare-earth nickelates," *Annu. Rev. Mater. Res.* **46**, pp. 305–334, 2016.

[24] S. Catalano, M. Gibert, J. Fowlie, J. Iniguez, J.-M. Triscone, and J. Kreisel, "Rare-earth nickelates $RNiO_3$: thin films and heterostructures," *Rep. Prog. Phys.* **81**(4), p. 046501, 2018.

[25] R. Jaramillo, S. D. Ha, D. Silevitch, and S. Ramanathan, "Origins of bad-metal conductivity and the insulator–metal transition in the rare-earth nickelates," *Nat. Phys.* **10**(4), p. 304, 2014.

[26] J. Zaanen, G. Sawatzky, and J. Allen, "Band gaps and electronic structure of transition-metal compounds," *Phys. Rev. Lett.* **55**(4), p. 418, 1985.

[27] T. Mizokawa, H. Namatame, A. Fujimori, K. Akeyama, H. Kondoh, H. Kuroda, and N. Kosugi, "Origin of the band gap in the negative charge-transfer-energy compound $NaCuO_2$," *Phys. Rev. Lett.* **67**(12), p. 1638, 1991.

[28] J. Alonso, M. Martínez-Lope, M. Casais, J. García-Muñoz, and M. Fernández-Díaz, "Room-temperature monoclinic distortion due to charge disproportionation in $RNiO_3$ perovskites with small rare-earth cations (R= Ho, Y, Er, Tm, Yb, and Lu): A neutron diffraction study," *Phys. Rev. B* **61**(3), p. 1756, 2000.

[29] D. Khomskii, "Unusual valence, negative charge-transfer gaps and self-doping in transition-metal compounds," *Lith. J. Phys.* **37**, p. 65, 1997.

[30] I. Mazin, D. Khomskii, R. Lengsdorf, J. Alonso, W. Marshall, R. Ibberson, A. Podlesnyak, M. Martínez-Lope, and M. Abd-Elmeguid, "Charge ordering as alternative to Jahn-Teller distortion," *Phys. Rev. Lett.* **98**(17), p. 176406, 2007.

[31] M. Medarde, C. Dallera, M. Grioni, B. Delley, F. Vernay, J. Mesot, M. Sikora, J. Alonso, and M. Martínez-Lope, "Charge disproportionation in $RNiO_3$ perovskites (R= rare earth) from high-resolution x-ray absorption spectroscopy," *Phys. Rev. B* **80**(24), p. 245105, 2009.

[32] H. Park, A. J. Millis, and C. A. Marianetti, "Site-selective mott transition in rare-earth-element nickelates," *Phys. Rev. Lett.* **109**(15), p. 156402, 2012.

[33] S. Johnston, A. Mukherjee, I. Elfimov, M. Berciu, and G. A. Sawatzky, "Charge disproportionation without charge transfer in the rare-earth-element nickelates as a possible mechanism for the metal-insulator transition," *Phys. Rev. Lett.* **112**(10), p. 106404, 2014.

[34] J. Varignon, M. N. Grisolia, J. Íñiguez, A. Barthélémy, and M. Bibes, "Complete phase diagram of rare-earth nickelates from first-principles," *npj Quantum Mater.* **2**(1), p. 21, 2017.

[35] V. Bisogni, S. Catalano, R. J. Green, M. Gibert, R. Scherwitzl, Y. Huang, V. N. Strocov, P. Zubko, S. Balandeh, J.-M. Triscone, G. Sawatzky, and T. Schmitt, "Ground-state oxygen holes and the metal-insulator transition in the negative charge-transfer rare-earth nickelates," *Nat. Commun.* **7**, p. 13017, 2016.

[36] R. J. Green, M. W. Haverkort, and G. A. Sawatzky, "Bond disproportionation and dynamical charge fluctuations in the perovskite rare-earth nickelates," *Phys. Rev. B* **94**(19), p. 195127, 2016.

[37] J. Shamblin, M. Heres, H. Zhou, J. Sangoro, M. Lang, J. Neuefeind, J. Alonso, and S. Johnston, "Experimental evidence for bipolaron condensation as a mechanism for the metal-insulator transition in rare-earth nickelates," *Nat. Commun.* **9**(1), p. 86, 2018.

[38] A. Mercy, J. Bieder, J. Íñiguez, and P. Ghosez, "Structurally triggered metal-insulator transition in rare-earth nickelates," *Nature communications* **8**(1), pp. 1–6, 2017.

[39] P. Hansmann, X. Yang, A. Toschi, G. Khaliullin, O. Andersen, and K. Held, "Turning a nickelate fermi surface into a cupratelike one through heterostructuring," *Phys. Rev. Lett.* **103**(1), p. 016401, 2009.

[40] D. Li, K. Lee, B. Y. Wang, M. Osada, S. Crossley, H. R. Lee, Y. Cui, Y. Hikita, and H. Y. Hwang, "Superconductivity in an infinite-layer nickelate," *Nature* **572**, pp. 624–627, 2019.

[41] J. Blasco, M. Castro, and J. Garcia, "Structural, electronic, magnetic and calorimetric study of the metal-insulator transition in $NdNiO_3$-delta," *J. Phys. Condens. Matter* **6**(30), p. 5875, 1994.

[42] J. Liu, M. Kargarian, M. Kareev, B. Gray, P. J. Ryan, A. Cruz, N. Tahir, Y.-D. Chuang, J. Guo, J. M. Rondinelli, *et al.*, "Heterointerface engineered electronic and magnetic phases of $NdNiO_3$ thin films," *Nat. Commun.* **4**, p. 2714, 2013.

[43] E. Mikheev, A. J. Hauser, B. Himmetoglu, N. E. Moreno, A. Janotti, C. G. Van de Walle, and S. Stemmer, "Tuning bad metal and non-Fermi liquid behavior in a Mott material: Rare-earth nickelate thin films," *Sci. Adv.* **1**(10), p. e1500797, 2015.

[44] H. Kobayashi, S. Ikeda, Y. Yoda, N. Hirao, Y. Ohishi, J. Alonso, M. Martinez-Lope, R. Lengsdorf, D. Khomskii, and M. Abd-Elmeguid, "Pressure-induced unusual metallic state in $EuNiO_3$," *Phys. Rev. B* **91**(19), p. 195148, 2015.

[45] E. Yadav, S. Harisankar, K. Soni, and K. Mavani, "Influence of Cu doping and thickness on non-Fermi liquid behaviour and metallic conductance in epitaxial $PrNiO_3$ thin films," *Appl. Phys. A* **124**(9), p. 614, 2018.

[46] V. E. Phanindra, P. Agarwal, and D. Rana, "Terahertz spectroscopic evidence of non-Fermi-liquid-like behavior in structurally modulated $PrNiO_3$ thin films," *Phys. Rev. Mater.* **2**(1), p. 015001, 2018.

[47] N. Hussey, K. Takenaka, and H. Takagi, "Universality of the Mott-Ioffe-Regel limit in metals," *Philos. Mag.* **84**(27), pp. 2847–2864, 2004.

[48] N. D. Patel, A. Mukherjee, N. Kaushal, A. Moreo, and E. Dagotto, "Non-fermi liquid behavior and continuously tunable resistivity exponents in the Anderson-Hubbard model at finite temperature," *Phys. Rev. Lett.* **119**(8), p. 086601, 2017.

[49] D. Preziosi, A. Sander, A. Barthélémy, and M. Bibes, "Reproducibility and off-stoichiometry issues in nickelate thin films grown by pulsed laser deposition," *AIP Adv.* **7**(1), p. 015210, 2017.

[50] M. Salamon, P. Lin, and S. H. Chun, "Colossal magnetoresistance is a Griffiths singularity," *Phys. Rev. Lett.* **88**(19), p. 1972013, 2002.

[51] J. Peng, C. Song, M. Wang, F. Li, B. Cui, G. Wang, P. Yu, and F. Pan, "Manipulating the metal-to-insulator transition of $NdNiO_3$ films by orbital polarization," *Phys. Rev. B* **93**(23), p. 235102, 2016.

[52] J. Bruin, H. Sakai, R. Perry, and A. Mackenzie, "Similarity of scattering rates in metals showing T-linear resistivity," *Science* **339**(6121), pp. 804–807, 2013.

[53] J. Bak, H. B. Bae, J. Kim, J. Oh, and S.-Y. Chung, "Formation of two-dimensional homologous faults and oxygen electrocatalytic activities in a perovskite nickelate," *Nano Lett.* **17**(5), pp. 3126–3132, 2017.

[54] C. Coll, L. López-Conesa, J. M. Rebled, C. Magén, F. Sanchez, J. Fontcuberta, S. Estrade, and F. Peiro, "Simulation of STEM-HAADF image contrast of Ruddlesden-Popper faulted $LaNiO_3$ thin films," *The Journal of Physical Chemistry C* **121**(17), pp. 9300–9304, 2017.

[55] L. López-Conesa, J. M. Rebled, D. Pesquera, N. Dix, F. Sánchez, G. Herranz, J. Fontcuberta, C. Magén, M. J. Casanove, S. Estradé, *et al.*, "Evidence of a minority monoclinic $LaNiO_{2.5}$ phase in lanthanum nickelate thin films," *Phys. Chem. Chem. Phys.* **19**(13), pp. 9137–9142, 2017.

[56] R. U. Chandrasena, W. Yang, Q. Lei, M. U. Delgado-Jaime, K. D. Wijesekara, M. Golalikhani, B. A. Davidson, E. Arenholz, K. Kobayashi, M. Kobata, *et al.*, "Strain-engineered oxygen vacancies in $CaMnO_3$ thin films," *Nano Lett.* **17**(2), pp. 794–799, 2017.

[57] F. Conchon, A. Boulle, R. Guinebretière, C. Girardot, S. Pignard, J. Kreisel, F. Weiss, E. Dooryhée, and J.-L. Hodeau, "Effect of tensile and compressive strains on the transport properties of $SmNiO_3$ layers epitaxially grown on (001) $SrTiO_3$ and $LaAlO_3$ substrates," *Appl. Phys. Lett.* **91**(19), p. 192110, 2007.

[58] S. Catalano, M. Gibert, V. Bisogni, O. Peil, F. He, R. Sutarto, M. Viret, P. Zubko, R. Scherwitzl, A. Georges, *et al.*, "Electronic transitions in strained $SmNiO_3$ thin films," *APL Mater.* **2**(11), p. 116110, 2014.

[59] A. Malashevich and S. Ismail-Beigi, "First-principles study of oxygen-deficient $LaNiO_3$ structures," *Phys. Rev. B* **92**(14), p. 144102, 2015.

[60] L. Wang, S. Dash, L. Chang, L. You, Y. Feng, X. He, K.-j. Jin, Y. Zhou, H. G. Ong, P. Ren, *et al.*, "Oxygen vacancy induced room-temperature metal–insulator transition in nickelate films and its potential application in photovoltaics," *ACS Appl. Mater. Interfaces* **8**(15), pp. 9769–9776, 2016.

[61] A. J. Hauser, E. Mikheev, N. E. Moreno, J. Hwang, J. Y. Zhang, and S. Stemmer, "Correlation between stoichiometry, strain, and metal-insulator transitions of $NdNiO_3$ films," *Appl. Phys. Lett.* **106**(9), p. 092104, 2015.

[62] L. Iglesias, A. Sarantopoulos, C. Magén, and F. Rivadulla, "Oxygen vacancies in strained $SrTiO_3$ thin films: Formation enthalpy and manipulation," *Phys. Rev. B* **95**(16), p. 165138, 2017.

[63] G. Herranz, V. Laukhin, F. Sánchez, P. Levy, C. Ferrater, M. García-Cuenca, M. Varela, and J. Fontcuberta, "Effect of disorder on the temperature dependence of the resistivity of $SrRuO_3$," *Phys. Rev. B* **77**(16), p. 165114, 2008.

[64] C. Ederer and N. A. Spaldin, "Influence of strain and oxygen vacancies on the magnetoelectric properties of multiferroic bismuth ferrite," *Phys. Rev. B* **71**(22), p. 224103, 2005.

[65] U. Aschauer, R. Pfenninger, S. M. Selbach, T. Grande, and N. A. Spaldin, "Strain-controlled oxygen vacancy formation and ordering in $CaMnO_3$," *Phys. Rev. B* **88**(5), p. 054111, 2013.

[66] N. F. Mott, "Conduction in non-crystalline materials: Iii. localized states in a pseudogap and near extremities of conduction and valence bands," *Philos. Mag.* **19**(160), pp. 835–852, 1969.

[67] S. Issai, *Is hopping a science?: selected topics of hopping conductivity*, World Scientific, 2015.

[68] B.-X. Wang, S. Rosenkranz, X. Rui, J. Zhang, F. Ye, H. Zheng, R. Klie, J. F. Mitchell, and D. Phelan, "Antiferromagnetic defect structure in $LaNiO_{3-\delta}$ single crystals," *Phys. Rev. Mater.* **2**(6), p. 064404, 2018.